Proceedings of the Combustion Institute 40 (2024) 105348

Contents lists available at ScienceDirect

Proceedings of the Combustion Institute

journal homepage: www.elsevier.com/locate/proci

The influence of clustering in homogeneous isotropic turbulence on the ignition behavior of iron particles

Gabriel Thäter [a,*], Maurizio Carbone [b,c], Tien-Duc Luu [b], Oliver T. Stein [d], Bettina Frohnapfel [a]

[a] Institute of Fluid Mechanics, Karlsruhe Institute of Technology, Karlsruhe, Germany
[b] Theoretical Physics I, University of Bayreuth, Bayreuth, Germany
[c] Max–Planck-Institute for Dynamics and Self-organization, Göttingen, Germany
[d] Engler-Bunte-Institute - Chair for Simulation of Reacting Thermo-Fluid Systems, Karlsruhe Institute of Technology, Karlsruhe, Germany

ARTICLE INFO

Keywords:
Iron combustion
Ignition
HIT
Euler–Lagrange
CP-DNS
Particle clustering
Voronoi tessellation

ABSTRACT

We conduct carrier-phase direct numerical simulations (CP-DNS) to investigate the ignition of iron particles in homogeneous isotropic turbulence, and characterize the connection between particle clustering and particle ignition. A pseudo-spectral reacting multiphase flow solver using a low Mach number approximation is employed. It features an established point-particle sub-model for reacting iron particles and describes the mass, heat and momentum transfer across the particle boundary layers in a two-way coupled regime. Within this setup, we perform a series of simulations covering a broad range of Reynolds and Stokes numbers. The results confirm the well-known observation from incompressible dispersed multiphase flows that particle clustering is most pronounced for particle clouds with Stokes numbers of order one. Here, strong particle clustering additionally facilitates the earlier ignition of heterogeneously burning iron particles. This is because groups of neighboring particles locally deposit more heat per volume than a single isolated particle, thus more strongly increasing the local fluid temperature and shifting particle reactions from kinetically-limited to diffusion-limited particle conversion. A Voronoi tessellation analysis shows that the particles packed together in clusters tend to ignite first, even for small Stokes numbers, at which clustering is less prominent. An increase in Reynolds number reduces the ignition delay times, especially for high Stokes numbers, since particles with higher inertia are more sensitive to the larger scales of the turbulent motion. The present findings are of practical importance for the design and flame stabilization mechanisms in future iron combustion burners.

1. Introduction

The growing energy demand driven by global industrial expansion, coupled with the adverse environmental effects of conventional fossil fuels, necessitates a shift towards large-scale renewable energy production. Globally, in 2021 only 17.7% of primary energy was derived from non-fossil sources [1], and many countries in e.g. central Europe heavily rely on energy imports due to geographical limitations on the potential for renewable energy. A promising concept for storing and transporting renewable energy is based on metal fuels. The key idea consists of a metal oxidation/reduction cycle, in which solar or wind energy is used to reduce e.g. pulverized iron oxide [2]. The resulting iron powder can be stored and safely transported over long distances [3]. Later, the iron is burned with air to release thermal energy which can be used for electricity generation in refitted coal power plants [4]. The iron combustion process is expected to be similar to the thermal conversion of conventional liquid or solid hydrocarbon fuels which are burned in a turbulent environment for increased efficiency. However, different from spray or coal combustion, where major parts of the fuel first evaporate or devolatilize and then burn in the gas phase, the reaction from iron to iron oxide mostly occurs heterogeneously. The mechanism of evaporation, which is essential for hydrocarbon combustion, is not as relevant for iron [5,6]. Therefore, even though particle or droplet combustion under turbulent flow conditions has been studied for hydrocarbon fuels [7–9], the behavior of coal and biomass in turbulent flows does not directly compare to iron combustion.

Several experiments and numerical simulations investigated the combustion behavior of single iron particles [5,10–12]. A common approach for large scale simulations reduces the combustion of each individual particle to a set of ordinary differential equations, modeling internal oxygen diffusion, heat conduction and iron reaction as zero-dimensional processes [12–15]. Some of those models have been used in one-dimensional flame solvers [15,16], but the combustion of iron particles in three-dimensional turbulent flows has not yet been studied systematically.

* Corresponding author.
E-mail address: gabriel.thaeter@kit.edu (G. Thäter).

https://doi.org/10.1016/j.proci.2024.105348
Received 5 December 2023; Accepted 4 June 2024
Available online 24 June 2024

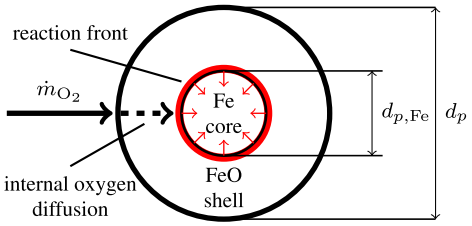

Fig. 1. Particle model with external and internal oxygen fluxes. Both the external diffusion $\dot{m}_{O_2}$ and the kinetics in the reaction front can be rate-limiting.

In the present work, we focus on the ignition behavior of iron particle clouds in homogeneous isotropic turbulence (HIT), which has not been studied in the archival literature before, to the best of the authors' knowledge. For non-reacting particles in incompressible flows, it is known that inertial particles tend to form clusters at various scales depending on their Stokes number, and small-scale clustering is more pronounced for Stokes numbers of order one [17,18]. The major objective of the present work is to relate the particle clustering to the particle ignition in iron particle clouds by means of high-resolution direct numerical simulations, with emphasis on the effect of Stokes and Reynolds numbers. The flow setup of homogeneous isotropic turbulence can provide fundamental insights on these effects.

2. Modeling

We model the particle combustion in a turbulent flow with an Euler–Lagrange CP-DNS approach. Our modeling of the fluid phase relies on the assumption that the flow-induced pressure fluctuations do not change thermodynamic quantities due to low Mach numbers [19], such that the pressure can be split into two parts

$$p(x,t) = p_0(t) + \pi(x,t). \tag{1}$$

The local pressure changes π due to momentum changes are small compared to p_0, such that material parameters of the fluid only depend on the spatially constant thermodynamic pressure p_0. The iron particles have a slip velocity and a temperature difference with respect to the surrounding fluid, which generates a two-way heat, mass and momentum transfer. A 0D iron combustion model is applied. The large density ratio between the particles and the gas phase, up to four orders of magnitude, justifies the assumption of a zero-dimensional particle model without volume displacement. During combustion, the iron is in a solid or liquid state, while the surrounding air is a gas. Following existing models in literature the reaction takes place solely in the particle, and the evaporation of iron is neglected [5,6].

2.1. Thermodynamic fluid model

The fluid phase consists of a mixture of the two ideal gases, oxygen (O_2) and nitrogen (N_2), governed by the state equation

$$p_0 = \rho R_M T. \tag{2}$$

Since the thermodynamic pressure $p_0(t)$ is constant throughout the domain due to the Low-Mach number assumption, the local density $\rho(x_i,t)$ can be calculated from the local temperature $T(x_i,t)$ and the mixture gas constant R_M, determined with the oxygen mass fraction Y_{O_2}. Due to the considerable temperature variations induced in the gas phase by the igniting particles, the model encompasses the consequent substantial changes of the thermodynamic quantities, e.g. thermal conductivity, heat capacity and viscosity, as functions of the local temperature and pressure. The heat capacity c_p and the specific enthalpy h of the fluid are computed as 5th and 6th order polynomial functions of the temperature [20]. For the thermal conductivity λ, we use the correlation introduced in [21],

$$\frac{\lambda}{c_p} = 2.58\times10^{-5}\,\mathrm{kg\,m^{-1}\,s^{-1}}\left(\frac{T}{298\,\mathrm{K}}\right)^{0.7}. \tag{3}$$

Finally, the dynamic viscosity μ of the fluid and the oxygen mass diffusivity D_{O_2} are calculated as

$$\mu = Pr\frac{\lambda}{c_p} \qquad D_{O_2} = \frac{\lambda Pr}{c_p \rho Sc_{O_2}}, \tag{4}$$

with constant Prandtl Pr and Schmidt number Sc_{O_2}.

2.2. Particle model

We use the iron particle combustion model introduced by Hazenberg & van Oijen [15], modeling only the main reaction from pure iron (Fe) to Wüstite (FeO). Later oxidation stages to Fe_3O_4 or Fe_2O_3 have a much lower energy deposition compared to the first stage. They form mainly during cooldown, so later in the single particle combustion process. Hence further oxidation is neglected in the present study on early ignition, to keep the particle model simple. Restricting ourselves to these early stages of the process, we assume that also evaporation of iron and its oxides is negligible and therefore do not include it in our model. The particle is assumed to consist of an iron core and an oxide shell, as illustrated in Fig. 1.

During reaction, the iron core shrinks and eventually vanishes, leading to an inert iron oxide particle. The energy set free by the exothermic oxidation heats up the particle, which subsequently cools down due to heat exchange with the surrounding gas phase. Due to our focus on ignition, the reactive cooling phase of the particles [6] is ignored to keep the model complexity low. The particle is assumed to be at a uniform temperature, due to the fast heat conduction in the particle compared to the convective heat exchange with the surrounding fluid (i.e., particles have a low Biot number). Therefore, the particle thermodynamics is expressed in terms of three variables: the total particle mass m_p, the mass of the iron core $m_{p,Fe}$, and the particle enthalpy H_p. The time evolution of those particle thermodynamics variables is described by a set of ordinary differential equations

$$\frac{\mathrm{d}m_p}{\mathrm{d}t} = \rho|_{x_p} Y_{O_2} A_d k_d Da^* \tag{5a}$$

$$\frac{\mathrm{d}m_{p,Fe}}{\mathrm{d}t} = -\frac{1}{s}\frac{\mathrm{d}m_p}{\mathrm{d}t} \tag{5b}$$

$$\frac{\mathrm{d}H_p}{\mathrm{d}t} = -k_c A_p (T_p - T|_{x_p}) + \frac{\mathrm{d}m_p}{\mathrm{d}t} h_{O_2}, \tag{5c}$$

where the subscript p denotes particle variables, while the subscript x_p indicates fluid variables evaluated at the particle position.

In the model Eqs. (5), the oxygen mass fraction Y_{O_2}, the diffusion surface A_d and the mass transfer coefficient through diffusion $k_d = ShD_{O_2,f}/d_{p,Fe}$ affect the particle mass change, while the normalized Damköhler number $Da^* = (A_r k_r)/(A_r k_r + A_d k_d)$ kinetically limits the reaction rate for small particle temperatures [15]. The reactive transfer rate is defined as $k_r = k_\infty \exp(-T_a/T)$, with k_∞ and T_a as constants. Following the assumption of a porous iron oxide shell, not inhibiting the oxygen diffusion to the core, identical diffusion and reaction surfaces of $A_r = A_d = \pi d_{p,Fe}^2$ are used. Due to the definition of Da^* and its parameters the range of the Damköhler number is always kept between 0 and 1. The parameter s in Eq. (5b) denotes the stoichiometric coefficient of the modeled Fe → FeO reaction. The particle enthalpy changes through a convective term driven by the temperature difference between the particle and the fluid. Also enthalpy exchange due to mass transfer with the surrounding fluid is possible, with h_{O_2} denoting the specific enthalpy of the oxygen in the gas phase. The particle temperature is connected to the enthalpy through

$$T_p = \frac{H_p + m_{p,FeO}\Delta h_c}{m_p c_{p,p}} + T_{h0}, \tag{6}$$

where Δh_c is the combustion enthalpy of the Fe-FeO reaction, and T_{h0} the temperature at zero enthalpy. Within particle clouds, the mean radiation absorption length $L_a = 1/(\pi r_p^2 N_P/L^3)$, gives a length scale for the exponential decrease of the radiation emitted by a single particle through absorption by other particles [22]. With the mean particle number density N_P/L^3 and the particle radius r_p considered in our study, the absorption length of $L_a \approx 1.4\,\mathrm{m}$ is much higher than the domain size, making the cloud optically thin. Therefore particle–particle heat transfer through radiation can be neglected. For the small particle diameters and temperature ranges considered, the convective heat transfer ($\propto d_p$) dominates over radiative heat losses ($\propto d_p^2$). Assuming a particle of $d_p = 10\,\mu\mathrm{m}$, an emissivity of 1 and particle temperatures of 2500 K in a surrounding fluid of $T = 800\,\mathrm{K}$, the radiative heat flux is less than 7% of the convective flux, so the influence of radiative heat losses during the preheating phase of iron particles is minor. Finally, the convection heat transfer coefficient is defined as $k_c = Nu\lambda_f/d_p$. Quantities with the subscript f are evaluated at the film temperature $T_f = T_p + (T|_{x_p} - T_p)/3$. For the Nusselt Nu (and Sherwood Sh) numbers used in k_d and k_c, we employ the correlation [23]

$$Nu = 2 + 0.6 Pr^{1/3} Re^{1/2}, \tag{7}$$

featuring the particle Reynolds number $Re_p = \|u_p - u|_{x_p}\| d_p/\nu_f$ and the constant Prandtl $Pr = 0.7$ (and Schmidt $Sc = 0.84$) numbers.

The particle momentum balance considers the Stokes drag force and the momentum exchange due to mass flux between the particle and the gas phase

$$\frac{\mathrm{d}u_{i,p}}{\mathrm{d}t} = -\frac{u_{i,p} - u_i|_{x_p}}{m_p}\left(3\pi\mu d_p + \frac{\mathrm{d}m_p}{\mathrm{d}t}\right). \tag{8}$$

2.3. Fluid flow model

Following the Low-Mach number assumption introduced in Section 2, the pressure fluctuation $\pi(x,t)$ appears in the momentum balance and is small compared to the thermodynamic pressure p_0. $\pi(x,t)$ is uniquely determined by the divergence of the fluid velocity field [19]. We fully resolve all scales of turbulence, therefore no turbulence model needs to be applied. Based on the low-Mach number assumption (1), the continuity, momentum and enthalpy equations for the gas phase read

$$\frac{\partial \rho}{\partial t} + \frac{\partial(\rho u_i)}{\partial x_i} = S_{\mathrm{O}_2} \tag{9a}$$

$$\rho\left(\frac{\partial u_i}{\partial t} + u_j\frac{\partial u_i}{\partial x_j}\right) = -\frac{\partial \pi}{\partial x_i} + \frac{\partial \tau_{ij}}{\partial x_j} + S_{\mathrm{u},i} + f_i \tag{9b}$$

$$\frac{\partial H}{\partial t} + \frac{\partial(u_i H)}{\partial x_i} = \frac{\partial}{\partial x_i}\left(\lambda\frac{\partial T}{\partial x_i}\right) + \frac{\mathrm{d}p_0}{\mathrm{d}t} + S_{\mathrm{H}}. \tag{9c}$$

where $u_i(x,t)$ is the fluid velocity, $f_i(x,t)$ an external forcing, $H(x,t)$ the volumetric enthalpy, and

$$\tau_{ij} = \mu\left(\frac{\partial u_i}{\partial x_j} + \frac{\partial u_j}{\partial x_i} - \frac{2}{3}\delta_{ij}\frac{\partial u_k}{\partial x_k}\right) \tag{10}$$

the stress tensor. The terms $S_\alpha(x,t)$ on the right-hand side of (9) denote the influence of the particles on the fluid. Owing to the point-particle assumption, this feedback of all N_P particles consists of a superposition of Dirac delta functions centered at the particle locations. The Fourier transform of such an irregular field can be well approximated through the Nonuniform Fast Fourier Transform [24]. The feedback field is calculated in physical space using a B-spline kernel, then transformed to Fourier space, where the convolution is reverted by dividing by the transform of the kernel. This provides a direct representation of the Dirac delta functions in Fourier space.

$$S_{\mathrm{O}_2} = -\sum_{n=1}^{N_p}\delta(x_i - x_{i,p})\dot{m}_{\mathrm{O}_2} \tag{11a}$$

$$S_{\mathrm{u},i} = -\sum_{n=1}^{N_p}\delta(x_i - x_{i,p})3\pi\mu d_p(u_i|_{x_p} - u_{i,p}) \tag{11b}$$

Table 1
Simulation setup.

N_F	L [cm]	$Re_{\lambda,0}$	η_0 [μm]	St_0	N_P
64	5.2	38	551	0.33	1 265 871
64	3.0	38	318	1.00	243 614
64	1.8	37	184	3.00	46 883
128	8.8	60	550	0.33	6 021 531
128	5.1	59	317	1.00	1 158 827
128	2.9	59	183	3.02	223 016
256	14.8	86	561	0.32	28 643 394
256	8.6	91	302	1.10	5 512 341
256	4.9	86	188	2.85	1 060 850

$$S_{\mathrm{H}} = -\sum_{n=1}^{N_p}\delta(x_i - x_{i,p})\frac{\mathrm{d}H_p}{\mathrm{d}t}. \tag{11c}$$

3. Simulation setup

We simulate the gaseous and particle phase in a two-way coupling regime using a pseudo-spectral solver [25], extended to incorporate considerable fluid density variations due to the combustion in a low-Mach number regime. The model Eq. (5), (8), (9) are integrated in time by using a two-step Runge–Kutta scheme with Courant–Friedrichs–Lewy number below 0.1. The simulation domain consists of a cube of edge length L, with periodic boundary conditions for both the particles and the fluid. The code resolves N_F Fourier modes in each direction, with maximum resolved wavenumber $k_{\max} = \pi N_F/L$. It employs the non-uniform Fast Fourier Transform [25,26] for the interpolation of the fluid variables at the particle position in Eq. (5),(8) and for the computation of the feedback terms (11). A large-scale stochastic forcing [27] keeps the velocity field at a statistically isotropic turbulent state. We have validated the implementation against reference data from literature [15] and another in-house solver [28].

We perform a total of nine simulations, at various Reynolds number based on the Taylor microscale,

$$Re_\lambda = \frac{\langle u_i u_i\rangle}{3}\sqrt{\frac{15}{\langle\nu\rangle\epsilon}}, \tag{12}$$

and particle Stokes number based on the Kolmogorov time scale

$$St = \frac{m_p}{3\pi\mu d_p}\sqrt{\frac{\epsilon}{\langle\nu\rangle}}. \tag{13}$$

where $\langle\cdot\rangle$ denotes the spatial average. The mean dissipation ϵ is defined as [29]

$$\epsilon = \frac{1}{\langle\rho\rangle}\left\langle\frac{\partial u_i}{\partial x_j}\tau_{ij}\right\rangle. \tag{14}$$

The simulations consist of two steps. First, we let the fluid flow without particles evolve into a statistically steady state, driven by the large-scale forcing, at a fluid temperature $T_0 = 800\,\mathrm{K}$. Second, we introduce N_P particles, initially randomly and uniformly distributed, with an initial diameter $d_{p,0} = 10\,\mu\mathrm{m}$ and initial velocity and temperature matching the fluid velocity and temperature at the particle position. By varying both the forcing magnitude (governing the average dissipation rate ϵ) and the domain length L, we can independently adjust the initial Reynolds number of the flow $Re_{\lambda,0}$ and the initial particle Stokes number St_0. The parameter space is constrained by the point-particle model hypotheses, requiring $k_{\max} d_p \ll 1$ [30], and by the accurate resolution of the smallest turbulent scales, down to the Kolmogorov length scale $\eta = (\langle\nu\rangle^3/\epsilon)^{1/4}$, requiring $k_{\max}\eta \gtrsim 2$. In the following the simulations are referred to as $Re_\lambda = 38$, 60, 88 and $St = 1/3$, 1, 3, and we report their characterizing parameters in Tables 1–3. The input parameters for the iron combustion model are mainly taken from [31]. We note that the activation temperature T_a is changed by $< 0.1\%$ for a slightly better match with the reference. A validation of the single particle model is

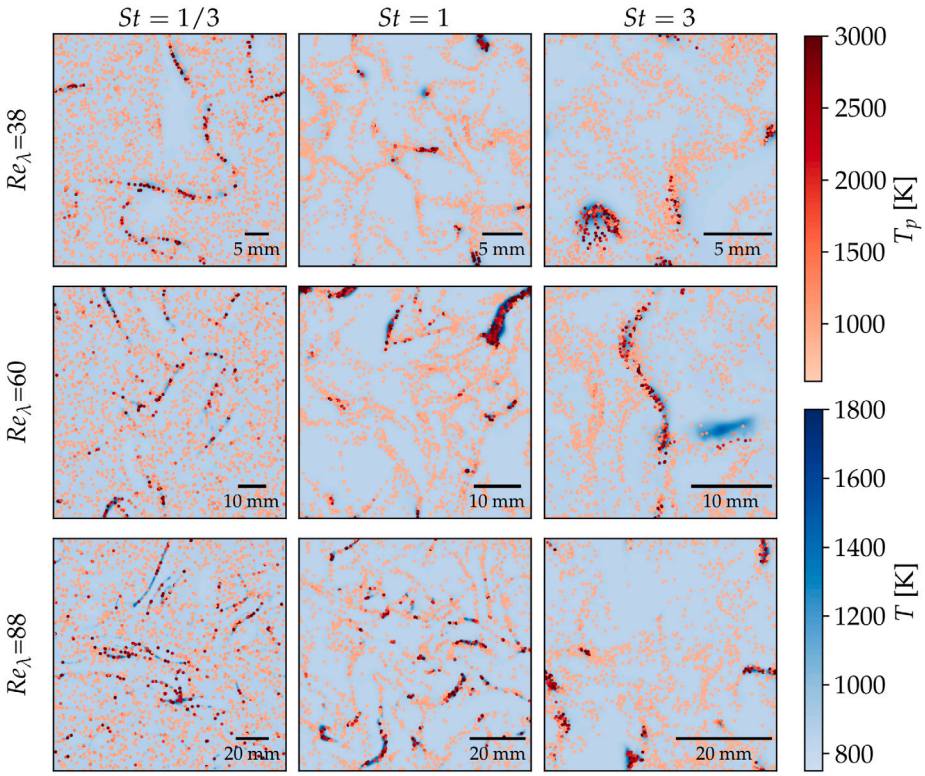

Fig. 2. 2D cuts from the different simulations when 10% of the particles have ignited. The individual plots are not to scale, the different domain lengths in each case are indicated by the scale in the subfigures.

Table 2
Thermodynamic parameters.

	Value	Unit
Y_{O_2}	0.2329	–
R_M	288.19	$\mathrm{J\,kg^{-1}\,K^{-1}}$
p_0	1×10^5	$\mathrm{N\,m^{-2}}$
Pr	0.7	–
Sc_{O_2}	0.84	–

Table 3
Iron combustion parameters.

	Value	Unit
ρ_{Fe}	7874	$\mathrm{kg\,m^{-3}}$
ρ_{FeO}	5745	$\mathrm{kg\,m^{-3}}$
$c_{p,p}$	667	$\mathrm{J\,kg^{-1}\,K^{-1}}$
k_∞	7.5×10^6	$\mathrm{m\,s^{-1}}$
T_a	14 412.5	K
s	0.27	–
Δh_c	2921×10^3	$\mathrm{J\,kg^{-1}}$

provided in the supplementary material. The number of particles N_P is such that the global equivalence ratio in the entire domain is very lean ($\phi = 0.1$). However, due to particle clustering ϕ locally reaches stoichiometric or even rich conditions, as we will show next.

4. Results and discussion

4.1. Particle clustering and ignition

Starting from the temperature of the surrounding fluid, the particles heat up due to an initially slow, kinetically-limited reaction. When the particles reach a critical temperature, they heat up significantly faster, indicating thermal runaway with the iron particles reacting in the oxygen diffusion-limited regime, as discussed in [15]. The particle ignition point is defined as the maximum temperature rate of change $\mathrm{d}T_p/\mathrm{d}t$. Within the simulation time span, the fraction of already ignited particles increases from 0 at the start to 1 at the end since all the particles eventually ignite.

Fig. 2 shows two-dimensional (2D) cuts of the three-dimensional (3D) flow domain from the nine simulations, at the instant in time at which 10% of the particles have ignited. At this instance in time less than 3.6% of the particles have reached peak temperature such that the simplifying assumptions for an early ignition stage taken in the model formulation are reasonable. From left to right St increases while Re_λ increases from top to bottom. The fluid and the particles located on the visualized slice are colored depending on their temperature. The three columns in Fig. 2 qualitatively differ, indicating a pronounced Stokes number effect. For $St = 1/3$ the particles cluster on scales comparable to the smallest scale of the flow, while the distribution appears comparably homogeneous on the largest scales. The visualizations at $St = 1$ display significant particle clustering coexisting with extended regions at low particle number density. Particle clusters are also visible in the right column for $St = 3$. In contrast to $St = 1$ however, the clustering appears to happen at larger length scales, i.e. the clustered regions are broader. This observation is in agreement with literature on incompressible turbulence, where clustering is found to be most prominent for $St = 1$ [17], and to take place at scales at which the particle Stokes number based on the scale-dependent eddy turnover is of order one [32]. Therefore, particles tend to cluster on a variety of scales, preferentially larger at larger Stokes numbers, making ignition and subsequent discrete flame propagation an intrinsically multiscale phenomenon. The multiscale nature of the inertial particle dynamics immediately relates to the effect of the Reynolds number. For increasing Re_λ, the clustering structures become more fine grained (compared to the domain size) reflecting the increased range of scales in the turbulent flow.

The particle clustering affects the ignition mechanism one-to-one since clustered particles markedly heat up the surrounding fluid thus

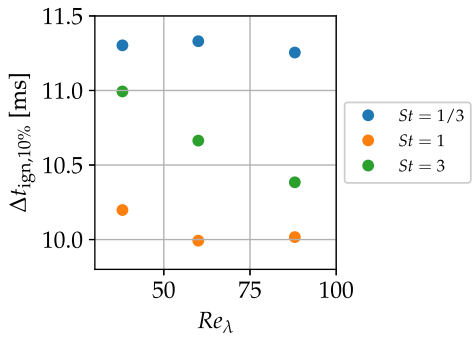

Fig. 3. Ignition delay time $\Delta t_{\mathrm{ign},10\%}$, defined between the start of the simulation and the time when 10% of all particles have ignited.

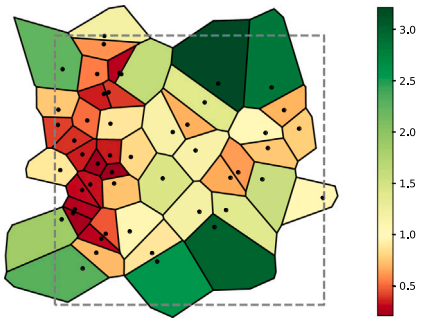

Fig. 4. 2D example of Voronoi tessellation with periodic boundary conditions. The patches are colored by the normalized area (volume in 3D).

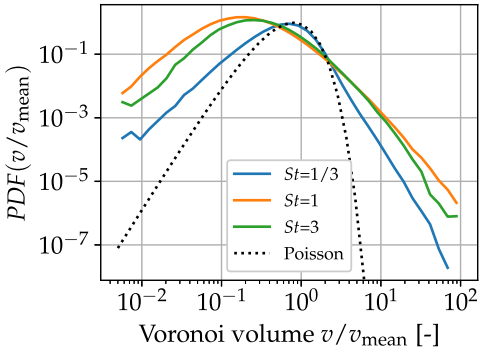

Fig. 5. Probability density function (PDF) of normalized Voronoi volumes for $Re_\lambda = 60$ cases when 10% of the particles have ignited. The dotted line shows the PDF for random uniformly distributed particles [34].

facilitating the ignition of the neighboring particles. Particles ignite for all the presented simulation setups, but at different preferential separations throughout the domain. At the smallest Stokes number, ignition takes place on thin small-scale streaks where more particles are close together. At $St = 1$, the ignition almost solely takes place within the particle clusters, thus strongly increasing the fluid temperature only at a few specific regions. For the largest St, the hot ignited particles appear to be located in larger-scale streaks. In all the cases, the number of different ignition locations increases at larger Re_λ for all Stokes numbers, which reflects the larger scale separation in the flow field.

4.2. Ignition delay time

In the following, we define the ignition delay time $\Delta t_{\mathrm{ign},10\%}$ between the start of the simulation and the instant in time at which 10% of the initially homogeneously distributed particles have ignited (i.e. the ones visualized in Fig. 2). The corresponding results are summarized in Fig. 3, showing that $\Delta t_{\mathrm{ign},10\%}$ differs for all investigated cases. Most prominent is its dependence on the Stokes number. The smallest ignition delay is found for $St = 1$ and the largest for $St = 1/3$ with time differences of more than 1 ms. For most cases, higher Re_λ leads to earlier ignition. This effect is most prominent for $St = 3$, and weakest for $St = 1/3$, consistent with the effects of Re_λ on the particle clustering discussed above. For $St = 1$, a slight increase of ignition time for $Re_\lambda = 88$ is observed. This change might be related to the randomness of the turbulent clustering and it is small compared to the change observed between $Re_\lambda = 38$ and $Re_\lambda = 60$. A comparison with Fig. 2 indeed suggests that particle clustering, most prominent for $St = 1$, is associated with faster ignition. The increased scale separation with increasing Re_λ is most effective for $St = 3$ where wide particle streaks can be broken up into smaller structures. The reduced ignition delay with increasing Re_λ can thus be interpreted as an effect of increased mixing which is most effective for large-scale particle clusters. In the following, this qualitative observation is complemented by a quantitative clustering analysis.

4.3. Clustering analysis by voronoi tessellation

To quantitatively investigate particle clusters, different methods exists, like box-counting and particle pair functions. We use a 3D Voronoi tessellation of the particle phase [8,9,18], which enables the use of global statistics and local analysis without prescribing any length scale a priori. Fig. 4 shows a 2D example of the analysis. Each particle is associated with a cell comprising the space region closer to that particle than to any other particle. In the 3D case, the volume of each cell gives a measure of the particle clustering: the smaller the Voronoi volume, the more clustered the particles are. More details about clustering analysis and the Voronoi tessellation in particular are provided in the supplementary material. We perform the tessellation into Voronoi volumes with the freud Python package [33], featuring periodic boundary conditions, as exemplified in Fig. 4.

The probability density function (PDF) of the Voronoi volumes normalized by the respective mean value is shown in Fig. 5 for various Stokes numbers at $Re_\lambda = 60$. The dashed line shows the Poisson distribution for randomly scattered particles [34]. The deviation from the random uniform distribution characterizes clustering. For a Stokes number of 1/3, the curve is similar to the reference Poisson distribution, whereas the PDFs for $St = 1$ and $St = 3$ display heavy tails for both very small and very large volumes. This is in agreement with the qualitative analysis of Fig. 2. Small Voronoi volumes correspond to particles within clusters while large Voronoi volumes indicate the presence of volumes with very low particle number density. The heavy tails of the PDF for $St = 1$ thus confirm that the strongest clustering is present for this case, followed by the case with $St = 3$. The curves for $Re_\lambda = 38$ and 88 visually match the ones shown in Fig. 5 and are therefore omitted in the plot for better readability.

We now quantify the observation regarding Fig. 2 that regions with clustered particles ignite earlier than regions with less particles, by considering the relation between particle temperature and the local Voronoi volume. Fig. 6 shows the corresponding scatter plots at $\Delta t_{\mathrm{ign},1\%}$ and $\Delta t_{\mathrm{ign},10\%}$ at $Re_\lambda = 60$ and for the three different Stokes numbers. The color code reflects the combustion progress in terms of the iron oxide mass fraction $Y_{\mathrm{FeO}} = m_{p,\mathrm{FeO}}/m_p$ of each particle. Particles in clusters appear on the left side of the plot and the vertical dotted line marks the mean Voronoi value. Interestingly, all three St cases show a remarkable similarity for an ignition rate of 1% (top row). Basically all ignited particles have a Voronoi volume smaller than the average volume, thus lying in clustered regions of the domain. This indicates that even for $St = 1/3$, which features the most homogeneous particle distribution and the largest ignition delay times, the particle ignition starts in clustered regions of the turbulent flow field. This preferred

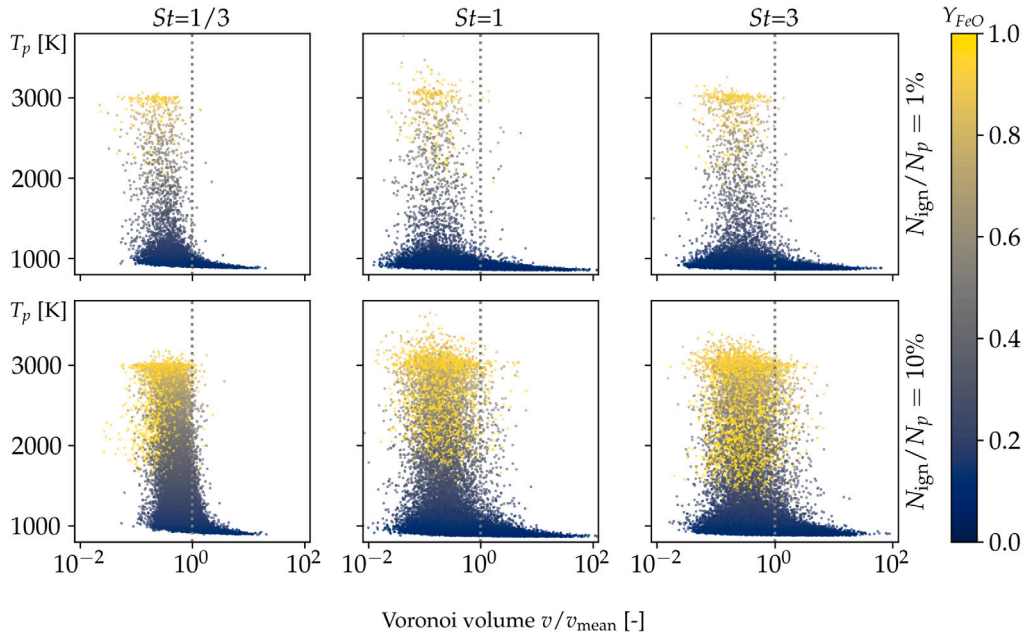

Fig. 6. Particle scatter plot at 1 (top row) and 10% ignited particles (bottom row) for $St = 1/3$, 1, 3 and $Re_\lambda = 60$. Particles in clusters will have a smaller Voronoi volume and be further on the left. They ignite earlier than particles outside clusters.

ignition in clustered regions can be linked to the larger local heat flux at high particle number densities. There the particle and surrounding fluid temperatures are increasing faster, leading to earlier ignition.

When the ignition rate reaches 10%, only a few particles outside the clustered regions have ignited, as shown in Fig. 6. The comparably large number of particles with high temperatures and large Voronoi volumes $v/v_{\text{mean}} > 1$ at $St = 1$ and $St = 3$ are likely to be caused by two different reasons. First, igniting particles located at the edge of clusters can have relatively large Voronoi volumes. Second, particles with a larger Stokes number can have a higher slip velocity due to the larger inertia compared to the fluid. This can enhance the heat fluxes from the clusters to regions with smaller particle number density, since fluid might move through hot particle groups, carrying the heat to regions with less particles. Those will be heated up and eventually ignite. Indications for both phenomena can be found in the visualization of Fig. 2, especially for the $St = 3$, $Re_\lambda = 60$ case in the mid right a hot fluid streak displaced from the combusting particle cluster is visible.

Since clustered particles ignite first for all St, the different ignition delay times in Fig. 3 can be explained by the PDF of the Voronoi volumes in Fig. 5. The presence of small volumes is the driving mechanism for small ignition delay: A large probability of small normalized Voronoi volumes (e.g. 0.1 and below) corresponds to a significantly shorter ignition time delay.

5. Conclusion

We have characterized the effect of particle clustering on the ignition of iron particle clouds in homogeneous isotropic turbulence by means of carrier-phase direct numerical simulation, at various Stokes numbers, $St = 1/3$, 1, 3 and Taylor Reynolds numbers $Re_\lambda = 38$, 60 and 88. In all the nine cases, particles ignite around 10 to 11.5 ms after the start of the simulation. In agreement with literature data for non-reactive turbulent particle flow the strongest particle clustering is observed at $St = 1$. This coincides with the smallest ignition delay times for the iron particles. In contrast, the $St = 1/3$ cases reveal less clustering and the longest ignition delay. Characterizing the clustering effect with a Voronoi tessellation allows to identify a strong correlation between clustering and ignition delay in the present study. A reduced ignition delay for particle clusters is physically reasonable, due to the larger local heat output by the particle phase. For high local particle concentrations, the critical temperature at which the iron reaction changes from kinetically to diffusion limited is reached earlier within hot particle streaks, so denser particle clusters lead to smaller ignition delay. An increase in Reynolds number shifts the ignition to earlier times for particles with significant inertia ($St = 1$ and 3), caused by increased separation between the largest and smallest length scales of the flow.

This work addressed the ignition phase of turbulent iron combustion. As a next step, we will use similar simulation setups to investigate the full combustion process, also at higher fuel equivalence ratios, as well as ignition propagation through cold iron-air-mixtures. Further model improvements target the inclusion of melting, evaporation and iron conversion to higher oxidation states. These results provide useful indicators for the design of future iron combustion burners.

Novelty and Significance Statement

• Metal oxidation/reduction fuel cycle is a promising concept for the transition to a carbon-free energy supply. • Detailed numerical study on iron particle ignition in homogeneous isotropic turbulence with varying Stokes and Reynolds number. • Particle clustering occurs in the flow depending on the Stokes number and strongly impacts the ignition delay. • The Reynolds number of the turbulent flow impacts ignition delay most in case of prominent particle clustering. • The obtained fundamental results are useful for the future design of iron combustion burners.

CRediT authorship contribution statement

Gabriel Thäter: Software, Validation, Formal analysis, Visualization, Writing. **Maurizio Carbone:** Software, Validation, Formal analysis, Writing. **Tien-Duc Luu:** Software, Validation. **Oliver T. Stein:** Conceptualization, Supervision, Writing – review & editing. **Bettina Frohnapfel:** Conceptualization, Supervision, Funding acquisition, Writing – review & editing.

Declaration of competing interest

The authors declare that they have no known competing financial interests or personal relationships that could have appeared to influence the work reported in this paper.

Acknowledgments

This work is conducted within the *Clean Circles* research initiative financially supported by KIT Strategiefonds. The authors gratefully acknowledge the financial support by the Helmholtz Association of German Research Centers, Germany (HGF), within the research field *Energy*, program *Materials and Technologies for the Energy Transition (MTET)*, topic *Resource and Energy Efficiency*. The authors also acknowledge support by the state of Baden-Württemberg, Germany through bwHPC.

Appendix A. Supplementary data

Supplementary material related to this article can be found online at https://doi.org/10.1016/j.proci.2024.105348.

References

[1] British Petrol, Statistical Review of World Energy 2022, seventy first ed., BP, London, 2022.
[2] J. Bergthorson, S. Goroshin, M. Soo, P. Julien, J. Palecka, D. Frost, D. Jarvis, Direct combustion of recyclable metal fuels for zero-carbon heat and power, Appl. Energy 160 (2015) 368–382.
[3] J. Neumann, R.C. da Rocha, P. Debiagi, A. Scholtissek, F. Dammel, P. Stephan, C. Hasse, Techno-economic assessment of long-distance supply chains of energy carriers: Comparing hydrogen and iron for carbon-free electricity generation, Appl. Energy Combust. Sci. 14 (2023) 100128.
[4] J. Janicka, P. Debiagi, A. Scholtissek, A. Dreizler, B. Epple, R. Pawellek, A. Maltsev, C. Hasse, The potential of retrofitting existing coal power plants: A case study for operation with green iron, Appl. Energ. 339 (2023) 120950.
[5] D. Ning, Y. Shoshin, M. van Stiphout, J. van Oijen, G. Finotello, P. de Goey, Temperature and phase transitions of laser-ignited single iron particle, Combust. Flame 236 (2022) 111801.
[6] A. Fujinawa, L.C. Thijs, J. Jean-Philyppe, A. Panahi, Di Chang, M. Schiemann, Y.A. Levendis, J.M. Bergthorson, X. Mi, Combustion behavior of single iron particles, part II: A theoretical analysis based on a zero-dimensional model, Appl. Energy Combust. Sci. 14 (2023) 100145.
[7] M. Rieth, A. Kempf, A. Kronenburg, O. Stein, Carrier-phase DNS of pulverized coal particle ignition and volatile burning in a turbulent mixing layer, Fuel 212 (2018) 364–374.
[8] P. Weiss, S.R. Bhopalam, D.W. Meyer, P. Jenny, On droplets that cluster and evaporate in reactive turbulence, Phys. Fluids 33 (3) (2021) 033322.
[9] G. Chen, H. Wang, K. Luo, J. Fan, A DNS study of pulverized coal combustion in a hot turbulent environment: Effects of particle size, mass loading and preferential concentration, Combust. Flame 254 (2023) 112839.
[10] D. Ning, Y. Shoshin, J. van Oijen, G. Finotello, L. de Goey, Burn time and combustion regime of laser-ignited single iron particle, Combust. Flame 230 (2021) 111424.
[11] L. Thijs, C. van Gool, W. Ramaekers, J. van Oijen, L. de Goey, Resolved simulations of single iron particle combustion and the release of nano-particles, Proc. Combust. Inst. 39 (3) (2023) 3551–3559.
[12] X. Mi, A. Fujinawa, J. Bergthorson, A quantitative analysis of the ignition characteristics of fine iron particles, Combust. Flame 240 (2022).
[13] S. Goroshin, M. Bidabadi, J. Lee, Quenching distance of laminar flame in aluminum dust clouds, Combust. Flame 105 (1) (1996) 147–160.
[14] A.E. Sidorov, V.G. Shevchuk, Laminar flame in fine-particle dusts, Combust. Explos. Shock Waves 47 (5) (2011) 518–522.
[15] T. Hazenberg, J. van Oijen, Structures and burning velocities of flames in iron aerosols, Proc. Combust. Inst. 38 (3) (2021) 4383–4390.
[16] J. Mich, D. Braig, T. Gustmann, C. Hasse, A. Scholtissek, A comparison of mechanistic models for the combustion of iron microparticles and their application to polydisperse iron-air suspensions, Combust. Flame 256 (2023) 112949.
[17] J. Bec, L. Biferale, M. Cencini, A. Lanotte, S. Musacchio, F. Toschi, Heavy particle concentration in turbulence at dissipative and inertial scales, Phys. Rev. Lett. 98 (2007) 084502.
[18] M. Momenifar, A.D. Bragg, Local analysis of the clustering, velocities, and accelerations of particles settling in turbulence, Phys. Rev. Fluids 5 (2020) 034306.
[19] R.G. Rehm, H.R. Baum, The equations of motion for thermally driven, buoyant flows, J. Res. Natl. Bur. Stand. 83 (3) (1978) 297–308.
[20] B.J. Mcbride, S.D. Gordon, M.A. Reno, Coefficients for calculating thermodynamic and transport properties of individual species, 1993.
[21] M.D. Smooke, Reduced Kinetic Mechanisms and Asymptotic Approximations for Methane-Air Flames, Springer Berlin, 1991.
[22] M. Liberman, Combustion Physics: Flames, Detonations, Explosions, Astrophysical Combustion and Inertial Confinement Fusion, 2021, pp. 481–482.
[23] W. Ranz, W. Marshall, Evaporation from drops, Chem. Eng. Prog. 48 (1952) 141–146.
[24] M. Carbone, M. Iovieno, Application of the nonuniform fast fourier transform to the direct numerical simulation of two-way coupled particle laden flows, WIT Press (2018) 237–248.
[25] M. Carbone, A.D. Bragg, M. Iovieno, Multiscale fluid–particle thermal interaction in isotropic turbulence, J. Fluid Mech. 881 (2019) 679–721.
[26] G. Beylkin, On the fast Fourier transform of functions with singularities, Appl. Comput. Harmon. Anal. 2 (4) (1995) 363–381.
[27] V. Eswaran, S. Pope, An examination of forcing in direct numerical simulations of turbulence, Comput. & Fluids 16 (3) (1988) 257–278.
[28] G. Thäter, M. Carbone, V. Venugopal, T.D. Luu, O.T. Stein, B. Frohnapfel, The influence of turbulence on micron-sized iron particle combustion, 2023, 31. Deutscher Flammentag, Berlin.
[29] V. Canuto, Compressible turbulence, Astrophys. J. 482 (2) (1997) 827.
[30] J.A.K. Horwitz, A. Mani, Two-way coupled particle-turbulence interaction: Effect of numerics and resolution on fluid and particle statistics, Phys. Rev. Fluids 5 (2020) 104302.
[31] T. Hazenberg, An Eulerian-Lagrangian approach for simulating heterogeneous combustion of metal fuels, 2019, De Zaale, Eindhoven.
[32] A.D. Bragg, P.J. Ireland, L.R. Collins, Mechanisms for the clustering of inertial particles in the inertial range of isotropic turbulence, Phys. Rev. E 92 (2015) 023029.
[33] V. Ramasubramani, B.D. Dice, E.S. Harper, M.P. Spellings, J.A. Anderson, S.C. Glotzer, freud: A software suite for high throughput analysis of particle simulation data, Comput. Phys. Comm. 254 (2020) 107275.
[34] J.-S. Ferenc, Z. Néda, On the size distribution of Poisson Voronoi cells, Phys. A 385 (2) (2007) 518–526.